Effect of shaping on Trapped Electron Mode stability: an analytical model

Xavier Garbet, Donnel P., Gianni L. De, Qu Z., Melka Y., Sarazin Y., Grandgirard V., Obrejan K., Bourne E., Dif-Pradalier G.

Effect of shaping on Trapped Electron Mode stability: an analytical model.

X. Garbet[1,2], P. Donnel[1], L. De Gianni[1], Z. Qu[2], Y. Melka[1], Y. Sarazin[1], V. Grandgirard[1], K. Obrejan[1], E. Bourne[3], G. Dif-Pradalier[1]
[1] CEA, IRFM, F-13108 Saint Paul-lez-Durance, France.
[2] School of Physical and Mathematical Sciences, Nanyang Technological University, 637371 Singapore.
[3] SCITAS, EPFL, CH-1015 Lausanne, Switzerland

e-mail contact of main author: xavier.garbet@ntu.edu.sg

Abstract . A reduced model for Trapped Electron Mode stability has been developed, which incorporates basic effects of magnetic surface shaping, in particular elongation and triangularity. This model shows that while elongation is stabilising, though weakly, negative triangularity usually leads to a more unstable plasma. This is in marked contrast with the experimental evidence of a better confinement at negative triangularity, and with recent gyrokinetic linear simulations. This paradox is solved when finite orbit and/or finite mode width effects are included. These effects give more weight to particles trapped at low bounce angles, which are the ones that exhibit lower precession frequencies at negative – as compared to positive – triangularity. As a result, the interchange growth rate becomes lower at negative triangularity and large temperature gradients, so that negative triangularity appears to have an overall stabilizing effect.

1 Introduction

Improving confinement is an essential step on the path towards fusion energy. Shaping offers an attractive alternative to well documented recipes such as shear flows or electromagnetic effects combined with energetic ions. Effect of shaping on confinement is a complex process. Indeed, shaping changes metric elements in transport equations and hence on confinement [1], even at constant heat diffusivity. The analysis is here restricted to changes in stability and scales, hence growth rates and perpendicular wave numbers. Two shaping parameters are particularly scrutinised, namely elongation and triangularity.

Increasing plasma elongation is known to decrease the growth rate of ion temperature gradient driven modes (ITGs) [1, 2] - we note though that both elongation and triangularity were simultaneously changed in the latter work - and Trapped Electron Modes (TEMs) [3]. Destabilisation of ITGs was found for flat density profiles when using a fluid description [4]. Most of these stability studies were undertaken well above instability threshold. It turns out that the instability threshold of ITG modes depends weakly on elongation [2], a surprising observation. This property was recovered by Angelino et al [5] - dependence of threshold on shaping is reestablished when using the temperature gradient length defined in the equatorial plane. In all cases, a clear decrease of heat diffusivity is found with

elongation in turbulent regime, stronger than expected on the basis of linear stability [2, 5]. This was attributed to a beneficial role of zonal flows, itself related to a higher Rosenbluth-Hinton residual with elongation [6], though this explanation remains speculative to date.

The situation is even less clear for triangularity. Since the initial discovery of the beneficial effect of negative triangularity on confinement in TCV [7, 8], several theoretical and numerical works have been undertaken to elucidate the reasons for improvement. The favourable impact of negative triangularity on trapped electron modes (TEM) has been early identified linearly [9] and in simulations non linearly [10], then confirmed in [11] together with a strong role of zonal flows in non linear regime. Recent experiments on DIII-D suggest negative triangularity also improves ion confinement [12, 13, 14]. However, numerical analyses of ITG stability and turbulent transport are sometimes difficult to interpret [15] since a clear effect is seen only at very high negative triangularities. On the other hand, a recent numerical stability analysis indicates that negative triangularity is stabilising, provided magnetic shear is large enough [16]. Subsequent linear simulations confirm that negative triangularity improves confinement if magnetic shear is large enough [17], even in cases previously analysed in [15]. Moreover, it also appears that the radial shear of triangularity plays an important role. The Rosenbluth-Hinton residual was investigated by Singh and Diamond [18]. They found that negative triangularity lowers the RH residual, hence opposite to expectation since this suggests a lower level of zonal flows. The same study indicates that the fraction of trapped particles decreases when going from negative to positive triangularity, hence does not support the idea of enhanced TEM stability at negative triangularity on the basis of this criterion alone. The same authors also investigated the effect of shaping on mean $E \times B$ shear stabilisation, and found a rather complex behaviour [19], in particular a weaker shearing at the outboard mid-plane at negative triangularity.

In fact it appears that several contradictory ingredients come into play, making difficult a clear-cut conclusion. This is why it is instructive to derive a quasi-analytical model of stability for small scale modes, complemented by some estimate of quantities that come into play non linearly, namely flow generation and perpendicular wave number.

The objective of this work is to assess the effect of shaping on trapped electron modes (TEM) with the help of a reduced model. This model is inspired by previous analytical or numerical works on TEMs [20, 21, 22, 23, 24, 25, 26]. Various key quantities like bounce and precession frequencies, and also perpendicular wave numbers, are computed with a local magnetic equilibrium derived by Hegna [27, 28]. For axisymmetric configurations such as tokamaks, this class of solutions is similar to Miller's equilibria [29], itself derived from solutions of the Grad-Shafranov equation computed close to magnetic axis [30]. It bears the advantages of flexibility, and gives access to stability analysis in tokamaks while accounting for 3D effects such as magnetic perturbations [31]. This methodology is applied to the class of "Culham equilibria" [32, 33, 34] to assess the impact of shaping on TEM stability.

It appears that the simplest model (local dispersion relation), while predicting enhanced stability with elongation as expected, finds that negative triangularity is destabilising (see

sections 4.1 to 4.4). Stabilisation is found only when finite orbit width effect and mode structure are accounted for (sections 4.5 to 4.7). This agrees qualitatively with findings of Merlo and Jenko [16] while providing a physical understanding. In particular it is consistent with a stabilisation that occurs when magnetic shear is large enough.

The remainder of the paper is organised as follows. The geometry is introduced in section 2, the shaping being parametrized by elongation and triangularity. Its consequences on the magnetic drift velocity and associated frequencies is detailed in section 3. The reduced model for the TEM instability is presented in the last section 4, together with the outcomes of the associated dispersion relations when accounting for various refinements, in particular finite orbit width effects and mode localisation.

2 Magnetic field near a reference magnetic surface

2.1 Magnetic field representation

It is well known that as long as the magnetostatic force balance condition $\mathbf{J} \times \mathbf{B} = \nabla p$ is satisfied (p pressure, $\mathbf{B}$ magnetic field, and $\mathbf{J}$ current density), and thus $\mathbf{B} \cdot \nabla p = 0$, the magnetic field can be written [35, 36]

$$\mathbf{B} = \nabla\alpha \times \nabla\psi$$

where ψ is the poloidal flux normalised to 2π, $\alpha = \zeta - q\theta$, and ζ is a toroidal angle, chosen here equal to minus the toroidal geometric angle, and θ a poloidal angle, thus defining a full set of magnetic flux coordinates (ψ, θ, ζ). This is in fact a contravariant representation of the magnetic field. Introducing the mapping $\mathbf{x}(\psi, \theta, \zeta)$, where $\mathbf{x}$ is the position vector, an equivalent expression of the magnetic field is therefore

$$\mathbf{B} = \frac{1}{\sqrt{g}} \left(q \frac{\partial \mathbf{x}}{\partial \zeta} + \frac{\partial \mathbf{x}}{\partial \theta} \right) \tag{1}$$

The gradient of the poloidal flux $\psi(\mathbf{x})$, normal to magnetic surfaces, is a function of poloidal and toroidal derivatives of the mapping $\mathbf{x}(\psi, \theta, \zeta)$, namely

$$\nabla\psi = \frac{1}{\sqrt{g}} \frac{\partial \mathbf{x}}{\partial \theta} \times \frac{\partial \mathbf{x}}{\partial \zeta} \tag{2}$$

Axisymmetry imposes a toroidal field of the form $I(\psi)\nabla\zeta$, so that the Jacobian reads

$$\sqrt{g} = \frac{1}{\mathbf{B} \cdot \nabla\theta} = \frac{qR^2}{I}$$

Let us introduce a reference magnetic surface, labelled by its poloidal flux ψ_s , and parametrised by its major radius $R_s(\theta)$, and altitude $Z_s(\theta)$. The position $\mathbf{x}_s$ of a point on the reference magnetic surface is

$$\mathbf{x}_s = R_s \hat{\mathbf{e}}_R + Z_s \hat{\mathbf{e}}_Z$$

where $\hat{\mathbf{e}}_R$ and $\hat{\mathbf{e}}_Z$ are unit vectors in the horizontal and vertical directions. The magnetic field on the reference magnetic surface, noted $\mathbf{B}_s$, and the poloidal flux gradient, noted $\nabla\psi_s$ are then given by Eqs.(1, 2) applied to $\mathbf{x} = \mathbf{x}_s$. In the same way, the Jacobian $\sqrt{g_s}$ reads

$$\sqrt{g_s} = \frac{q_s R_s^2}{I_s}$$

where q_s is the safety factor on the magnetic surface, and I_s is a constant current that is written $I_s = B_\Delta R_\Delta$, with B_Δ the toroidal magnetic field at the reference radius $R = R_\Delta$.

It is desirable to determine the magnetic field in the vicinity of this reference magnetic surface. Following Hegna [27, 28], a Taylor development provides the mapping that relates the position vector $\mathbf{x}$ to its value on the reference magnetic surface

$$\mathbf{x}(\psi, \theta, \zeta) = \mathbf{x}_s(\theta, \zeta) + \mathbf{x}'_s(\theta, \zeta)(\psi - \psi_s) + o(\psi - \psi_s)^2$$

The displacement $\mathbf{x}'_s$ is conveniently expressed as

$$\mathbf{x}'_s = hB_s\mathbf{b} + \frac{1}{|\nabla\psi_s|}\mathbf{n} + D_H\frac{|\nabla\psi_s|}{B_s}\boldsymbol{\tau} \tag{3}$$

where h and D_H are functions of (θ, ζ), and $\mathbf{b} = \mathbf{B}_s/B_s$ is the unit tangent vector to the field on the reference surface, $\mathbf{n} = \nabla\psi_s/|\nabla\psi_s|$ the unit vector normal to the reference magnetic surface (the notation $\nabla\psi_s$ has to be understood as $\nabla\psi$ calculated at $\psi = \psi_s$), and $\boldsymbol{\tau} = \mathbf{b} \times \mathbf{n}$ a binormal unit vector, thus defining a Darboux frame. This set of unit vectors is a variant of the Frenet basis (in the Frenet basis, the normal unitary vector $\boldsymbol{\kappa}_c$ is such that, by definition: $(\mathbf{b}\cdot\nabla)\mathbf{b} = \boldsymbol{\kappa}_c$. The curvature $\boldsymbol{\kappa}_c$ should not be confused with the elongation κ) that satisfies the following set of relations

$$\begin{aligned}
(\mathbf{b}\cdot\nabla)\mathbf{b} &= \kappa_n\mathbf{n} + \kappa_g\boldsymbol{\tau} \\
(\mathbf{b}\cdot\nabla)\mathbf{n} &= -\kappa_n\mathbf{b} + \tau_r\boldsymbol{\tau} \\
(\mathbf{b}\cdot\nabla)\boldsymbol{\tau} &= -\kappa_g\mathbf{b} - \tau_r\mathbf{n}
\end{aligned}$$

The normal and geodesic curvatures κ_n, κ_g, and relative torsion τ_r are fully determined by the mapping $\mathbf{x}_s(\theta, \zeta)$, and are therefore considered as given.

The coefficient of $\mathbf{n}$ in Eq.(3) is set by the condition $\nabla\psi \cdot \frac{\partial\mathbf{x}}{\partial\psi}\Big|_s = 1$. Hence two functions $h(\theta, \zeta)$ and $D_H(\theta, \zeta)$ remain to be calculated, given the magnetostatic force balance condition $\mathbf{J} \times \mathbf{B} = \nabla p$ (the pressure p is a magnetic flux function), and Ampère equation $\nabla \times \mathbf{B} = \mu_0\mathbf{J}$. Moreover, the h and D_H functions are related in axisymmetric equilibria, since the metric element $\frac{\partial\mathbf{x}}{\partial\zeta} \cdot \frac{\partial\mathbf{x}}{\partial\psi}$ vanishes, hence $\nabla\zeta \cdot \mathbf{x}'_s = 0$. Plugging Eq.(3) in this constraint, an expression

$$h = \frac{|\nabla\psi_s|^2}{\sqrt{g_s}q_s R_s^2 B_s^2} D_H$$

is found that relates h and D_H [27, 28] - hence only the D_H function is needed. Still following closely Hegna [27, 28], the function D_H is given by the following relationship

$$(\mathbf{B}_s \cdot \nabla) D_H = \frac{1}{\sqrt{g_s}} \frac{dq_s}{d\psi} + \frac{B_s^2}{|\nabla \psi_s|^2} S_s \tag{4}$$

where $S_s = \boldsymbol{\tau} \cdot \nabla \times \boldsymbol{\tau}$ is the local magnetic shear, related to the average parallel current density $\sigma_s = \mu_0 \frac{\langle \mathbf{J}_s \cdot \mathbf{B}_s \rangle_{\psi_s}}{\langle B_s^2 \rangle_{\psi_s}}$ and pressure gradient via the relation

$$S_s = \sigma_s + \frac{dp_s}{d\psi} \lambda_H - 2\tau_r \tag{5}$$

and the function λ_H is given by the relation

$$(\mathbf{B}_s \cdot \nabla) \lambda_H = 2\kappa_g \mu_0 \frac{|\nabla \psi_s|}{B_s} \tag{6}$$

under the constraint $\langle \lambda_H B_s^2 \rangle_{\psi_s} = 0$. As pointed out by Hegna [28], the flux surface average of Eq.(4) yields a constraint that relates the average parallel current σ_s, average magnetic shear $\frac{dq_s}{d\psi}$ and pressure gradient $\frac{dp_s}{d\psi}$. Hence, as always in tokamak equilibrium calculations, two functions must be prescribed, which will be here the pressure gradient and the parallel current. Wrapping-up, given a mapping that prescribes a reference magnetic surface, plus average current and pressure gradient, a local equilibrium is computed by solving Eqs.(4) and (6) on functions λ_H and D_H. Once this is done all quantities of interest can be calculated, in particular bounce and precession frequencies, opening the path towards a full assessment of stability. The objective here is to determine conditions for stabilisation with elongation and triangularity.

2.2 Large aspect ratio class of equilibria

2.2.1 Mapping of a magnetic surface

Following [28], this methodology is now applied to the following mapping of the reference magnetic surface, inspired from [32, 33, 34],

$$\begin{aligned} R_s(\theta) &= R_\Delta + (r_s - E_s)\cos(\theta) + T_s \cos(2\theta) \\ Z_s(\theta) &= (r_s + E_s)\sin(\theta) - T_s \sin(2\theta) \end{aligned} \tag{7}$$

where R_Δ is a reference major radius and r_s a minor radius. E_s is related to the elongation κ_s and T_s to the triangularity δ_s via the relationships

$$E_s \simeq r_s \frac{\kappa_s - 1}{\kappa_s + 1} \qquad T_s \simeq r_s \frac{\delta}{4}$$

Note that these expressions are approximate: they hold for small values of $(\kappa_s - 1)$ and δ, and large aspect ratios. This equilibrium is reminiscent of the class of "Culham" shaped

global equilibria [32, 33, 34]. However it is stressed that θ denotes here a straight field line poloidal angle, hence different from the geometrical poloidal angle used in the class of "Culham" equilibria. Also no Shafranov shift is included in the mapping of the reference surface Eq.(7) since it is a local approximation, hence included in R_Δ.

Examples of magnetic surface cross-sections are shown in Fig.1 with parameters $r_s/R_\Delta = 0.3$, $\kappa_s = 1.5$ and $\delta_s = \pm 0.5$. For all plots below, the choice of safety factor and magnetic shear is $q_s = 3$, $s_s = 2$.

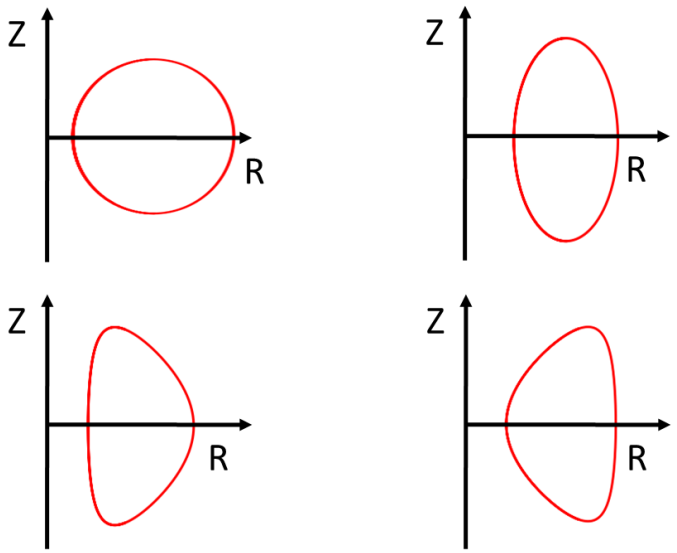

Figure 1: Shape of magnetic surfaces with a Culham equilibrium. top left: circular $\kappa_s = 1, \delta = 0$, top right: elongated $\kappa_s = 1.75, \delta = 0$, bottom left: positive triangularity $\kappa_s = 1.5, \delta_s = 0.5$ (left panel) bottom right: negative triangularity $\kappa_s = 1.5, \delta_s = -0.5$.

2.2.2 Local magnetic equilibrium

The full expressions of the functions λ_H and D_H are quite complex for a Culham equilibrium. They get simpler when using a large aspect ratio expansion, in the spirit of the initial derivation of this class of equilibria. A small expansion parameter is defined as $\epsilon = r_s/R_\Delta$. Let us define an effective θ-dependent minor radius a_s

$$a_s = \left[\left(\frac{\partial R_s}{\partial \theta} \right)^2 + \left(\frac{\partial Z_s}{\partial \theta} \right)^2 \right]^{1/2}$$

The minor radius r_s can be chosen as the poloidal average of the effective radius a_s over θ, so that $\partial_\theta R_s \sim \partial_\theta Z_s \sim r_s$, and also $E_s \sim T_s \sim r_s$. In the special case of a Culham equilibrium, r_s is chosen identical to the eponymous radius that appears in the mapping

$R_s(\theta), Z_s(\theta)$ at requested order in the ϵ expansion. The function λ_H is then given by the following expression

$$\lambda_H = -\frac{2\mu_0}{I_s} R_\Delta \left(r_s - E_s\right) \cos\theta + T_s \cos(2\theta)$$

where $I_s = B_s R_s$ is a constant at order 1 in ϵ.

Key parameters for the computation of the magnetic equilibrium are the magnetic shear

$$s_s = B_s \frac{r_s^2}{q_s^2} \frac{dq_s}{d\psi}$$

and MHD pressure parameter

$$\alpha_m = -2\mu_0 q_s r_s R_s \frac{1}{B_s} \frac{dp_s}{d\psi} \tag{8}$$

The function D_H is solution of Eq.(4), which involves the local shear Eq.(5). The analysis is restricted to the limit $\frac{dp_s}{d\psi}\lambda_H > |\sigma_s - 2\tau_r|$. In circular geometry where $\frac{s_s}{q_s R_\Delta} + \sigma_s - 2\tau_r = 0$, this is equivalent to $\alpha_m > s_s$. In this case the pressure prevails over parallel current and relative torsion in Eq.(5). This approximation, similar to the "$s-\alpha$ equilibrium", has been widely used, in particular to study ballooning mode stability [37] and "α-stabilisation" of ITG modes [38]. To illustrate the physics at play, we use here the special case $\alpha_m = 0$. The following expression is then found

$$D_H = \frac{q_s^2}{r_s^2 B_s} \alpha_m \tilde{D} \tag{9}$$

where

$$\frac{\partial \tilde{D}}{\partial \theta} = \tilde{k}(\theta)$$

with $\tilde{k} = k - \langle k \rangle_\theta$, and

$$k(\theta) = \frac{r_s^2}{a_s^2(\theta)} \tilde{R}_s(\theta)$$

where

$$a_s = \left(r_s^2 + E_s^2 + T_s^2 + 2r_s E_s \cos 2\theta + 4 r_s T_s \cos\theta + 4 E_s T_s \cos 3\theta\right)^{1/2}$$

In the circular limit, $\tilde{D} = \sin\theta$, as expected. Strictly speaking, magnetic shear s_s and pressure α_m parameters depend on the poloidal angle θ. However, at lowest order in ϵ, both can be considered as constant by replacing (R_s, B_s) by (R_Δ, B_Δ), and hence will be considered as given.

3 Magnetic drift velocity and precession frequency

Key ingredients to compute the drive of ITG modes are components of the magnetic drift velocity. The counterpart for TEMs is the precession frequency of trapped particles, which also depends on components of the magnetic drift velocity. Indeed the growth rate well above instability threshold for ITG/TEM modes is of the interchange type, i.e. is proportional to the square root of the precession frequency times the diamagnetic frequency.

3.1 Components of the magnetic drift velocity

The expression of the magnetic drift velocity for a species labelled "a" reads

$$\mathbf{v}_D = \frac{m_a v_\parallel^2}{e_a B}\mathbf{b}\times\boldsymbol{\kappa}_c + \frac{\mu}{e_a}\mathbf{b}\times\frac{\nabla B}{B}$$

where e_a is the species algebraic charge, and m_a its mass. An alternative expression is

$$\mathbf{v}_D = \frac{m_a v_\parallel^2 + \mu B}{e_a B}\mathbf{b}\times\boldsymbol{\kappa}_c - \frac{\mu}{e_a}\mathbf{b}\times\frac{\mu_0\nabla p}{B^2}$$

It is convenient to compute the contravariant components of the magnetic drift velocity $\mathbf{v}_D\cdot\nabla\psi$ and $\mathbf{v}_D\cdot\nabla\alpha$. The expressions derived in section Eq.(2.2.2) yield explicit expressions of the magnetic drift velocity components

$$\mathbf{v}_D\cdot\nabla\alpha = \frac{q_s}{e_a B_s r_s^2 R_s}\left[\left(m_a v_\parallel^2 + \mu B_s\right)\left(\frac{r_s^2}{a_s^2}\frac{\partial Z_s}{\partial\theta} - \left(s_s\theta - \alpha_m\tilde{D}\right)\frac{\partial R_s}{\partial\theta}\right) - \frac{\alpha_m\mu B_s}{2q_s^2}\right] \tag{10}$$

and

$$\mathbf{v}_D\cdot\nabla\psi = \frac{1}{q_s e_a R_s}\left(m_a v_\parallel^2 + \mu B_s\right)\frac{\partial R_s}{\partial\theta} \tag{11}$$

3.2 Precession frequency

3.2.1 Analytical expressions

There are two ways to compute the precession frequency. One way consists in expressing the parallel adiabatic invariant $J_\parallel$ as a function $\mathcal{J}$ of (μ, H, ψ)

$$\mathcal{J}(\mu, H, \psi) = \frac{1}{\pi}\int_{-\theta_b}^{\theta_b} d\ell\; m_a v_\parallel(\mu, H, \psi) \tag{12}$$

where H is the Hamiltonian, ψ the poloidal flux at the banana tip, μ the magnetic moment, and ℓ the curvilinear abscissa along a field line. It is also known that the Hamiltonian H is some function of the 3 invariants of motion $(\mu, J_\parallel, P_\zeta)$, where $P_\zeta = -e_a\psi$ is the toroidal kinetic momentum. The precession frequency is the partial derivative of the Hamiltonian

with respect to P_ζ, i.e. $\Omega_d = \left.\frac{\partial H}{\partial P_\zeta}\right|_{\mu,J_\parallel}$, at constant $(\mu, J_\parallel)$. Taking the derivative of Eq.(12) with respect to ψ with H considered as a function of $(\mu, J_\parallel, \psi)$, one gets the relation

$$\left.\frac{\partial \mathcal{J}}{\partial H}\right|_{\mu,\psi} \left.\frac{\partial H}{\partial \psi}\right|_{\mu,J_\parallel} + \left.\frac{\partial \mathcal{J}}{\partial \psi}\right|_{\mu,H} = 0 \tag{13}$$

which can be recast as

$$\Omega_d = \frac{1}{e_a} \frac{\left.\frac{\partial \mathcal{J}}{\partial \psi}\right|_{\mu,H}}{\left.\frac{\partial \mathcal{J}}{\partial H}\right|_{\mu,\psi}}$$

The second way is a direct calculation that involves the bounce average of the magnetic drift frequency, i.e.

$$\Omega_d = \frac{\int_{-\theta_b}^{\theta_b} \frac{d\ell}{v_\parallel} \mathbf{v}_D \cdot \nabla\alpha}{\int_{-\theta_b}^{\theta_b} \frac{d\ell}{v_\parallel}}$$

Both yield the same result, as they should, i.e.

$$\begin{aligned}
\left.\frac{\partial \mathcal{J}}{\partial \psi}\right|_{\mu,H} &= \frac{q_s}{r_s} \frac{1}{B_s R_s} \frac{1}{\pi} \int_{-\theta_b}^{\theta_b} d\theta \sqrt{g_s} \frac{B_s}{v_\parallel} \left(m_a v_\parallel^2 + \mu B_s\right) \\
&\qquad \left[\frac{r_s^2}{a_s^2} \frac{1}{r_s} \frac{\partial Z_s}{\partial \theta} - \left(s_s \theta - \alpha_m \tilde{D}\right) \frac{1}{r_s} \frac{\partial R_s}{\partial \theta}\right] \\
&- \frac{\alpha_m}{2q_s^2} \frac{q_s}{r_s} \frac{1}{B_s R_s} \frac{1}{\pi} \int_{-\theta_b}^{\theta_b} d\theta \sqrt{g_s} \frac{B_s}{v_\parallel} \mu B_s \\
\left.\frac{\partial \mathcal{J}}{\partial H}\right|_{\mu,\psi} &= \frac{1}{\pi} \int_{-\theta_b}^{\theta_b} d\theta \sqrt{g_s} \frac{B_s}{v_\parallel}
\end{aligned}$$

where θ_b is the bounce angle, see Eq.(14). The derivative $\left.\frac{\partial \mathcal{J}}{\partial H}\right|_{\mu,\psi}$ is also related to the bounce frequency Ω_b

$$\frac{1}{\Omega_b} = \left.\frac{\partial \mathcal{J}}{\partial H}\right|_{\mu,\psi} = \frac{1}{\pi} \int_{-\theta_b}^{\theta_b} d\theta \sqrt{g_s} \frac{B_s}{v_\parallel}$$

Let us note that for passing particles, the transit frequency, still noted Ω_b, reads

$$\frac{1}{\Omega_b} = \frac{1}{2\pi} \int_{-\pi}^{\pi} d\theta \sqrt{g_s} \frac{B_s}{v_\parallel}$$

Note the jump by a factor 2 at the passing/trapped boundary. The expression of Ω_d for passing particles is somewhat more intricate, and will not be given here, since passing electrons are not included in this model.

The bounce frequency is conveniently written in a separable form in energy and pitch-angle variable

$$\Omega_b = \bar{\Omega}_b(\lambda) \sqrt{\mathcal{E}} \frac{v_T}{2q_s R_{\max}}$$

with $\mathcal{E} = E/T$ the energy normalised to the temperature, and $v_T = \sqrt{T/m_a}$ a thermal velocity. Similarly the precession frequency is written

$$\Omega_d(\lambda) = \Omega_{dT}\bar{\Omega}_d(\lambda)\mathcal{E}$$

where

$$\Omega_{dT} = \frac{q_s}{r_s}\frac{T}{e_a B_s R_s}$$

The pitch-angle variable, defined below, is replaced whenever convenient by the bounce angle θ_b, such that

$$\begin{aligned} \lambda &= \frac{\mu B_{min}}{E} \\ &= \frac{1}{b_s(\theta_b)} = \frac{R_s(\theta_b)}{R_{max}} \end{aligned} \tag{14}$$

where $B_{min} = B_s(\theta = \pi)$ and b_s is the ratio $\frac{B_s}{B_{min}}$. Explicit expression for a Culham equilibrium are given in Appendix A.

3.2.2 Effect of shaping on precession frequency

Let us now analyse the impact of shaping on the precession frequency, keeping in mind that far above threshold, drive is proportional to the square root of the product of diamagnetic frequency with precession frequency. Hence the sign and amplitude of Ω_d as a function of the bounce angle θ_b is instructive. Parameters q_s, s_s and ϵ are given in Table 1.

Fig.2 compares circular ($\kappa = 1.0, \delta = 0$) and elongated ($\kappa = 1.75, \delta = 0$) configurations. The precession frequency decreases with increasing elongation (apart from the case of marginally trapped particles with $\theta_b \approx \pi$), thus indicating a decrease of the interchange drive. This observation is consistent with the fluid approach, and goes in the direction of improved confinement when the plasma elongation increases. This behaviour also agrees with the expectation from global scaling laws of confinement that also show enhanced confinement with elongation.

Fig.3 compares positive and negative triangularities $\delta = 0.5$ and $\delta = -0.5$ at vanishing MHD pressure parameter $\alpha_m = 0$. The precession frequency turns out to be smaller at negative than positive triangularity, in the range $\theta_b \lesssim 2$. One may argue that the interchange drive should be weighted by the fraction of trapped particles. However, this fraction scales as $\sqrt{R_s(\theta = \pi) - R_s(\theta = 0)}$ in a Culham equilibrium, and thus depends weakly on triangularity (second order in $T(r_s)/r_s$). It will be seen later on (cf. section 4.5 and the following ones) that a weight on deeply trapped particles results from finite orbit width effects, and also mode ballooning.

Hence the situation is rather intricate, since the effect of triangularity is not the same depending on the bounce angle, i.e. depending whether a particle is deeply or barely trapped. Negative δ is favorable for deeply trapped particles. However the effect reverses for barely trapped particles. Moreover, a fluid interchange drive is a poor indicator for a resonant instability driven by trapped particles. Hence the need for a better kinetic indicator.

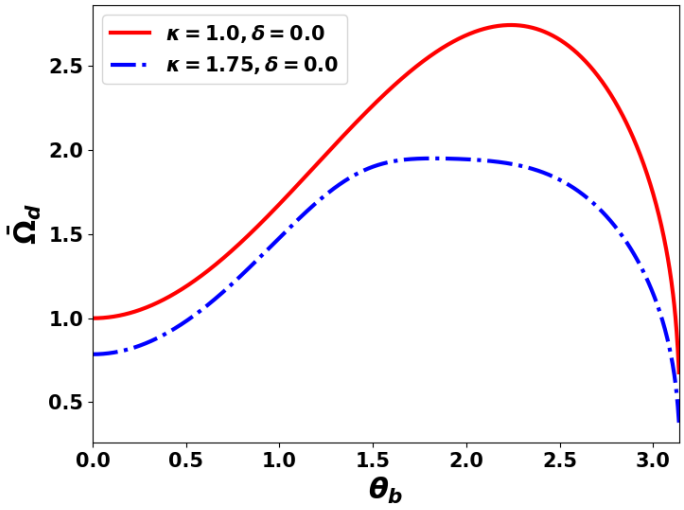

Figure 2: Precession frequency of trapped particles vs bounce angle θ_b for $\alpha_m = 0$ for circular $\kappa = 1.0$ (red) and elongated $\kappa = 1.75$ (blue) configuration at zero triangularity $\delta = 0$.

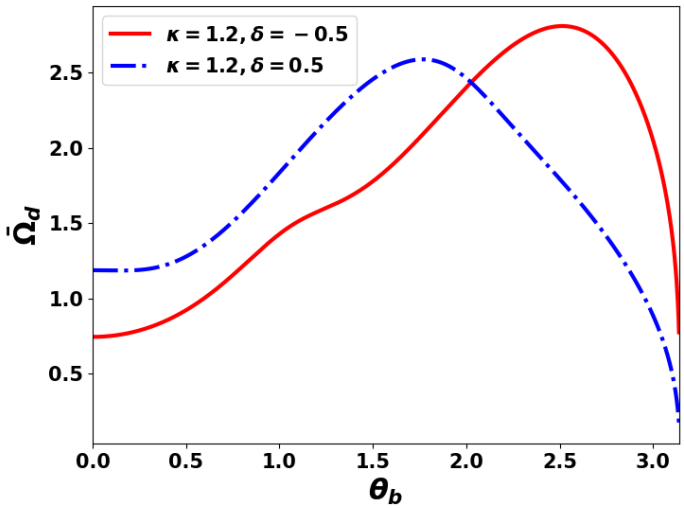

Figure 3: Precession frequency of trapped particles vs bounce angle θ_b for $\alpha_m = 0$, $\kappa = 1.2$ for positive $\delta = 0.5$ (blue) and negative $\delta = -0.5$ (red) triangularities.

4 A reduced kinetic model for trapped electron modes

4.1 Model description

A simple model for trapped electron modes is derived by assuming a Boltzman-like response for the perturbed ion density $\delta N_i = N_{eq}\, \Xi\, e_i \delta\phi / T_{i,eq}$ ($\delta\phi$ the perturbed electric

potential, N_{eq} the unperturbed density, e_i the ion charge), and also for passing electrons, while the response of trapped electrons is kinetic. Slef-consistency is ensured by a charge quasi-neutrality constraint $\delta N_e = \delta N_i$, where δN_e is the perturbed electron density, sum of trapped and passing contributions. In principle, Ξ is a complex function that depends on the mode frequency and wavenumber, and plasma parameters. In this model, it is a constant. This constant is zero in the limit of low wave numbers, and large frequencies - other choices can be made as long as Ξ is treated as a constant (e.g. $\Xi = 1$ in [20]). The price to pay is the impossibility to compute a mode structure, which requires a numerical solution. This procedure allows a computation of a local dispersion relation. This dispersion relation, written for an arbitrary species labelled "a", reads [20, 39]

$$\mathcal{L}(\omega) = 1 - f_t \left\langle \frac{\omega_{*T}\left(\mathcal{E} - \frac{3}{2} + \frac{1}{\eta}\right) - \omega}{\omega_d \mathcal{E} - \omega} \right\rangle_{\mathcal{E},\lambda} = 0 \tag{15}$$

where ω is the mode angular frequency, ω_{*T} the thermal diamagnetic frequency, $\eta = d\ln T_{eq}/d\ln N_{eq}$ (T_{eq} is the unperturbed temperature), and ω_d a magnetic drift frequency. The thermal diamagnetic frequency is defined as $\omega_{*T} = n\Omega_{*T}$, where n is the toroidal wave number, $\Omega_{*T} = -\frac{T_{eq}}{e_a}\frac{d\ln T_{eq}}{d\psi}$ (for TEMs, $e_a = -e$, where e is the proton charge). Similarly the magnetic drift frequency reads $\omega_d = \omega_{dT}\bar{\Omega}_d(\lambda)$, with $\omega_{dT} = n\Omega_{dT}$. The bracket is an average on both energy and pitch-angle

$$\langle ... \rangle_{\mathcal{E}} = \frac{2}{\sqrt{\pi}} \int_0^{+\infty} d\mathcal{E}\sqrt{\mathcal{E}} e^{-\mathcal{E}} ...$$

and

$$\langle ... \rangle_{\lambda} = \frac{1}{f_t} \int_{\lambda_-}^{\lambda_+} \frac{d\lambda}{\sqrt{2}\,\bar{\Omega}_b(\lambda)} ...$$

where f_t is the fraction of trapped particles

$$f_t = \int_{\lambda_-}^{\lambda_+} \frac{d\lambda}{\sqrt{2}\,\bar{\Omega}_b(\lambda)} \tag{16}$$

Here $\lambda_- = \frac{B_{min}}{B_{max}}$ and $\lambda_+ = 1$ are lower and upper-bounds of the trapped domain, while $\bar{\Omega}_b(\lambda)$ and $\bar{\Omega}_d(\lambda)$ are the normalised bounce and precession frequencies. Hence an explicit expression of the resonant part of the dispersion relation is

$$\left\langle \frac{\omega_{*T}\left(\mathcal{E} - \frac{3}{2} + \frac{1}{\eta}\right) - \omega}{\omega_d \mathcal{E} - \omega} \right\rangle_{\mathcal{E},\lambda} = \frac{1}{f_t} \int_{\lambda_-}^{\lambda_+} \frac{d\lambda}{\sqrt{2}\,\bar{\Omega}_b(\lambda)} \frac{2}{\sqrt{\pi}} \int_0^{+\infty} d\mathcal{E}\sqrt{\mathcal{E}} e^{-\mathcal{E}} \frac{\omega_{*T}\left(\mathcal{E} - \frac{3}{2} + \frac{1}{\eta}\right) - \omega}{\omega_{dT}\bar{\Omega}_d(\lambda)\mathcal{E} - \omega - i0^+}$$

4.1 Model description

It is reminded that the pitch-angle variable is unequivocally related to the bounce angle θ_b, Eq.(14). The diamagnetic frequency ω_{*T} does not depend explicitly on shaping, just on the temperature derivative with respect to the poloidal flux ψ. As a consequence the key stability parameter $\frac{\omega_{*T}}{\omega_{dT}}$ weakly depends on shaping. In the case of a Culham equilibrium, it is just the ratio $\frac{R_\Delta}{L_T}$, where L_T is a temperature gradient length $L_T^{-1} = -d\ln T_{eq}/dr$. We use the following normalisations

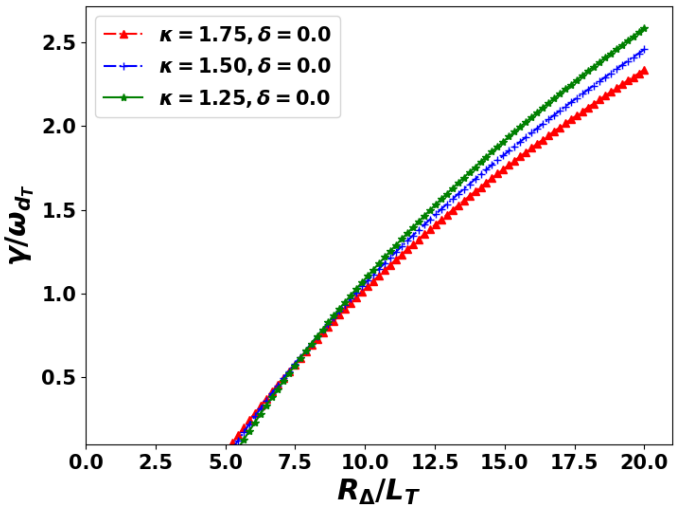

Figure 4: Growth rate vs R_Δ/L_T for three different values of elongation $\kappa = 1.25$, and $\kappa = 1.5$ and $\kappa = 1.75$ with null triangularity $\delta = 0$.

$$\epsilon_T = \frac{\omega_{dT}}{f_t \omega_{*T} \langle K_d \rangle_\lambda} \tag{17}$$

and

$$\Omega = \frac{\omega \langle K_d \rangle_\lambda}{\omega_{dT}} \tag{18}$$

where

$$K_d(\lambda) = \frac{1}{\bar{\Omega}_d(\lambda)}$$

and

$$k_d(\lambda) = \frac{K_d(\lambda)}{\langle K_d \rangle_\lambda} = \frac{\bar{\Omega}_d^{-1}(\lambda)}{\langle \bar{\Omega}_d^{-1} \rangle_\lambda}$$

The dispersion relation then reads

$$\mathcal{D}(\Omega) = \epsilon_T - 1 - \left\langle \left[\left(\Omega \left(k_d - f_t \epsilon_T \right) - \frac{3}{2} + \frac{1}{\eta} \right) \right] k_d G_{\epsilon_d} \left(\Omega k_d \right) \right\rangle_\lambda = 0 \tag{19}$$

where $\epsilon_d = \text{sign}(K_d)$. When multiplying the resonant function by the K_d function, one must be careful to change the Landau prescription accordingly, so that the function G_ϵ is defined as

$$G_\epsilon(\Omega) = \left\langle \frac{1}{\mathcal{E} - \Omega - i\epsilon} \right\rangle_{\mathcal{E}}$$

This notation means that when $\epsilon > 0$, the function G_ϵ is defined in the upper complex half-plane, and continued analytically in the lower half-plane of complex Ω, while for $\epsilon < 0$, one starts from the lower half-plane and performs an analytical continuation towards the upper-half plane. This implies that whenever Ω is a real and positive number Ω_r, the Landau prescription imposes

$$G_\epsilon(\Omega_r) = P.P. \left\langle \frac{1}{\mathcal{E} - \Omega_r} \right\rangle_{\mathcal{E}} + 2\text{sign}(\epsilon) i\sqrt{\pi}\Omega_r^{1/2} e^{-\Omega_r}$$

Details and properties of this function, in particular its expression in terms of the plasma dispersion function are given in Appendix B. The derivative of the dispersion relation function is

$$\begin{aligned} \frac{d\mathcal{D}}{d\Omega} &= -\left\langle \left(k_d - f_t\epsilon_T\right) k_d G_{\epsilon_d}\left(\Omega k_d\right)\right\rangle_\lambda \\ &- \left\langle \left[\left(\Omega\left(k_d - f_t\epsilon_T\right) - \frac{3}{2} + \frac{1}{\eta}\right)\right] k_d^2 G'_{\epsilon_d}\left(\Omega k_d\right)\right\rangle_\lambda \end{aligned}$$

where G'_{ϵ_d} is the derivative of G_{ϵ_d}, also derived in Appendix B.

4.2 Instability threshold

At marginal stability $\Omega = \Omega_r = \Re(\Omega)$, $\Im(\Omega) = 0$, the real frequency is solution of the following equation

$$\left\langle k_d^2 G_{\epsilon_d,i}(\Omega_r k_d)\right\rangle_\lambda \Omega_r = c_0 \left\langle k_d G_{\epsilon_d,i}(\Omega_r k_d)\right\rangle_\lambda \tag{20}$$

where $c_0 = \frac{3}{2} - \frac{1}{\eta} + f_t\epsilon_{T,crit}$. Eq.(20) is obtained by cancelling the imaginary part of the dispersion relation Eq.(19). Existence of a solution is not granted. However since all quantities are normalised, one may expect a solution $\Omega_r = O(1)$ – and in practice it is so. The real part of the dispersion relation yields the threshold $\epsilon_{T,crit}$

$$\epsilon_{T,crit} = 1 + \frac{c_0}{\left\langle k_d^2 G_{\epsilon_d,i}\right\rangle_\lambda}\left[\left\langle k_d^2 G_{\epsilon_d,r}\right\rangle_\lambda \left\langle k_d G_{\epsilon_d,i}\right\rangle_\lambda - \left\langle k_d G_{\epsilon_d,r}\right\rangle_\lambda \left\langle k_d^2 G_{\epsilon_d,i}\right\rangle_\lambda\right] \tag{21}$$

where all functions $G_{\epsilon_d,r}, G_{\epsilon_d,i}$ are computed at $\Omega_r k_d$.

Quite surprisingly, shaping does not change much the real frequency Ω_r, nor the threshold $\epsilon_{T,crit}$, which never departs much from 1. This is due to compensations in the integral Eq.(21) between moments of the k_d function. This property is verified as follows: if k_d is

not far from 1, say $k_d(\lambda) = 1 + e(\lambda)$, with $e \ll 1$, then corrections are of order e, more exactly

$$\epsilon_{T,crit} \simeq 1 + \frac{c_0}{\langle G_{\epsilon_d,i}\rangle_\lambda}\left[\langle eG_{\epsilon_d,r}\rangle_\lambda \langle G_{\epsilon_d,i}\rangle_\lambda - \langle G_{\epsilon_d,r}\rangle_\lambda \langle eG_{\epsilon_d,i}\rangle_\lambda\right] + \mathcal{O}(e^2) \tag{22}$$

At this point, one should avoid a hasty conclusion since Ω_r and $\epsilon_{T,crit}$ are not the actual frequency and threshold, but quantities normalised to parameters that depend on geometry. Hence a "de-normalisation" must be performed using Eqs.(17,18), more precisely

$$\frac{\omega}{\omega_{dT}} = \frac{\Omega}{\langle K_d\rangle_\lambda}$$

and

$$A_{T,crit} = \frac{1}{f_t \epsilon_{T,crit} \langle K_d\rangle_\lambda}$$

where $A_T = \frac{\omega_{*T}}{\omega_{dT}} = \frac{R_\Delta}{L_T}$. If the threshold is given by $\epsilon_{T,crit} \simeq 1$, then

$$A_{T,crit} \simeq \frac{1}{f_t \langle K_d\rangle_\lambda} \tag{23}$$

4.3 Solution well above instability threshold

The "hydrodynamic" limit of the dispersion relation is obtained via an expansion at large arguments Ω, and thus covers solutions with large growth rates. Using the asymptotic expression of the G_ϵ at large arguments Eq.(31), one finds

$$\begin{aligned}\mathcal{D}(\Omega) = (1-f_t)\,\epsilon_T &+ \left(\frac{1}{\eta} - \frac{3}{2} f_t \epsilon_T \left\langle \frac{1}{k_d}\right\rangle_\lambda\right)\frac{1}{\Omega} \\ &+ \frac{3}{2}\left[\left(1+\frac{1}{\eta}\right)\left\langle\frac{1}{k_d}\right\rangle_\lambda - \frac{5}{2} f_t\epsilon_T \left\langle\frac{1}{k_d^2}\right\rangle_\lambda\right]\frac{1}{\Omega^2} \\ &+ \frac{15}{4}\left[\left(2+\frac{1}{\eta}\right)\left\langle\frac{1}{k_d^2}\right\rangle_\lambda - \frac{7}{2} f_t\epsilon_T \left\langle\frac{1}{k_d^3}\right\rangle_\lambda\right]\frac{1}{\Omega^3} = 0\end{aligned}$$

Keeping the two first lines, one gets the usual fluid dispersion relation

$$\begin{aligned}(1-f_t)\,\epsilon_T\Omega^2 &+ \left(\frac{1}{\eta} - \frac{3}{2} f_t \epsilon_T \left\langle \frac{1}{k_d}\right\rangle_\lambda\right)\Omega \\ &+ \frac{3}{2}\left[\left(1+\frac{1}{\eta}\right)\left\langle\frac{1}{k_d}\right\rangle_\lambda - \frac{5}{2} f_t\epsilon_T \left\langle\frac{1}{k_d^2}\right\rangle_\lambda\right] = 0\end{aligned}$$

For a small fraction of trapped particles $f_t \to 0$ and vanishing density gradients $\eta \to \infty$, one recovers the interchange growth rate of TEMs

$$\gamma = \sqrt{\frac{3}{2}}\sqrt{f_t \omega_{dT}\omega_{*T}\left\langle\bar{\Omega}_d\right\rangle_\lambda} \tag{24}$$

q	s	ϵ	κ	α_m or β	R_Δ/L_N
3.0	2.0	0.16	1.2	0	4

Table 1: Parameters used to solve the dispersion relation.

A striking and paradoxical result emerges. The instability threshold is given by (from Eq.(23))

$$\frac{R}{L_{Tcr}} \simeq \frac{1}{f_t \left\langle \bar{\Omega}_d^{-1} \right\rangle_\lambda} \tag{25}$$

Well above the instability threshold, the growth rate behaves as Eq.(24). Suppose $\bar{\Omega}_d$ is proportional to some shaping parameter S. Then $\gamma \sim S^{0.5}$, while $\frac{R}{L_{Tcr}} \sim S$. So if shaping is stabilising well above threshold, it is destabilising near threshold in the sense it decreases the instability threshold – and vice-versa. Of course this rule of thumb is mitigated by the dependency of the fraction of trapped particles on shaping, and also shortcoming on averages, i.e. $1/\left\langle \bar{\Omega}_d^{-1} \right\rangle_\lambda \neq \left\langle \bar{\Omega}_d \right\rangle_\lambda$.

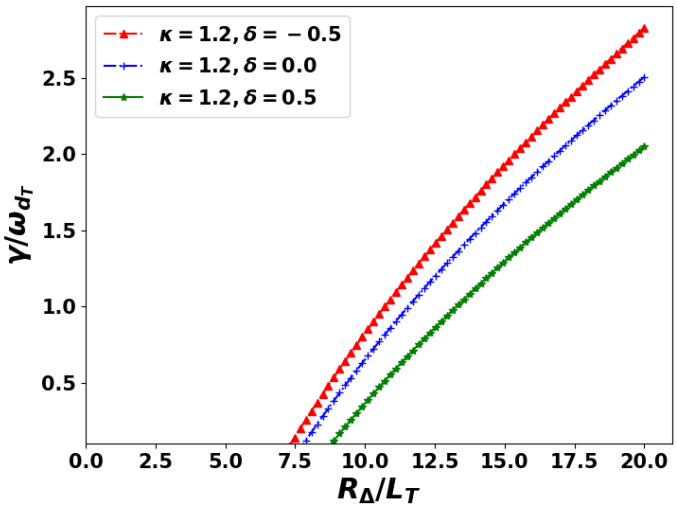

Figure 5: Growth rate vs R_Δ/L_T for a triangularity scan $\delta = -0.5$, $\delta = 0.0$ and $\delta = 0.5$ at fixed elongation $\kappa = 1.2$.

4.4 Numerical results

The dispersion relation has been solved numerically for parameters shown in Table 1 and for a fixed density gradient $R_\Delta/L_N = 4$, with $L_N^{-1} = -d\ln N_{eq}/dr$.

Solving numerically the dispersion relation brings several useful results:

- the instability threshold is quite close to the criterion $\epsilon_T = 1$ for all geometries hence Eq.(23) approximately holds.

- a favourable effect of elongation is recovered, but not very large, see Fig.4. This is consistent with [2, 5] for ITG modes. We note that curves cross. This is a consequence of the result found above: a stabilising effect near threshold becomes destabilising well above threshold, and vice-versa.

- *negative triangularity is found destabilising*, as shown in Fig.5.

This last result is of course unexpected. It is a consequence of the intricate shape of the precession frequency with bounce angle. A closer look at Fig.3 indicates that stabilisation must come from a smaller weight of barely trapped particles than predicted by this simple model. Different physical mechanisms can reduce the weight of barely trapped particles in the bounce angle integral, hence allowing to retrieve a stabilisation of negative triangularity. These mechanisms are investigated in the following sections.

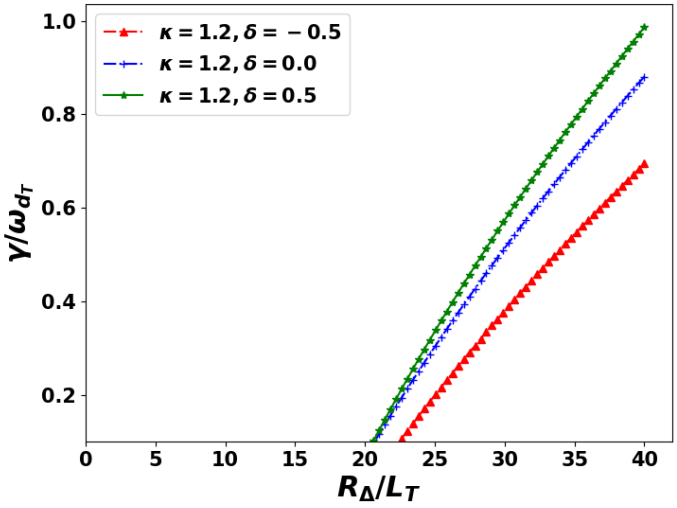

Figure 6: Growth rate vs R_Δ/L_T for a triangularity scan $\delta = -0.5$, $\delta = 0.0$ and $\delta = 0.5$ at fixed elongation $\kappa = 1.2$ with FOW effects included $C = 1.0$.

4.5 Adding finite orbit width effects

Using Appendix C, the dispersion relation that accounts for Finite Orbit Width (FOW) effects is of the form

$$1-\int_{\lambda_-}^{\lambda_+}\frac{d\lambda}{\sqrt{2}\bar{\Omega}_b(\lambda)}\frac{2}{\sqrt{\pi}}\int_0^{+\infty}d\mathcal{E}\sqrt{\mathcal{E}}e^{-\mathcal{E}}\frac{\omega_{*T}\left(\mathcal{E}-\frac{3}{2}+\frac{1}{\eta}\right)-\omega}{\omega_{dT}\bar{\Omega}_d(\lambda)\mathcal{E}-\omega-i0^+}J_0^2\left(C\sqrt{\mathcal{E}}\theta_b^2(\lambda)\right)=0$$

where $C=\frac{\delta_b}{2d}$, with $\delta_b=\frac{m_a}{e_a}v_T\left[R_\Delta\left(r_s-E_s+4T_s\right)\right]^{1/2}$ the banana width in ψ unit, and $d^{-1}=n\left.\frac{dq}{d\psi}\right|_{\psi=\psi_s}$ the inverse of the distance between resonant surfaces. Hence, one has

$$C=\frac{1}{2}q_s s_s k_\theta \rho_i\sqrt{\frac{m_e}{m_i}}\sqrt{\frac{1}{\epsilon}\left(1-\frac{E_s}{r_s}+4\frac{T_s}{r_s}\right)}$$

The parameter C turns out to be proportional to the poloidal wave number $k_\theta=nq_s/r_s$ and magnetic shear s (see derivation in Appendix C). The dispersion relation can be reshaped in a form identical to Eq.(19). Unfortunately energy/pitch-angle separability is lost. A new G function must be defined

$$G_\epsilon(\Omega,\theta_b)=\left\langle J_0^2\left(C\sqrt{\mathcal{E}}\theta_b^2\right)\frac{1}{\mathcal{E}-\Omega-i\epsilon}\right\rangle_{\mathcal{E}}$$

which will now enter bounce angle averages. All normalised quantities remain the same.

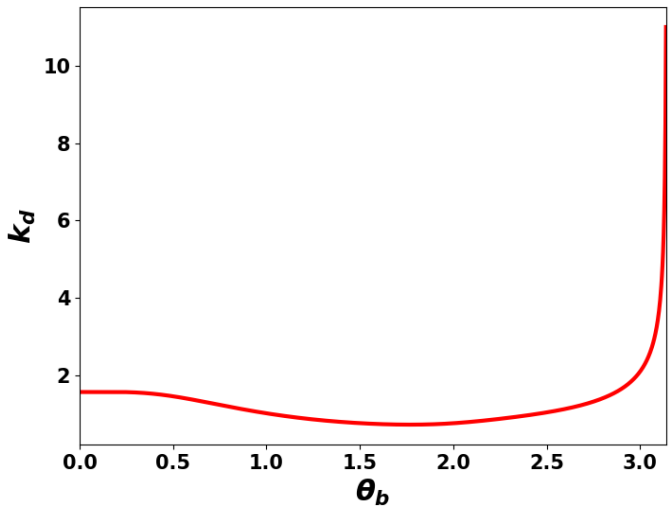

Figure 7: Function k_d vs θ_b for $\kappa=1.5$ and $\delta=0.5$.

Solving numerically this new relation dispersion shows that a negative triangularity is now stabilising, see the case $C=1.0$ in Fig.6. As an indication, the choice of parameters

$k_\theta \rho_{Ti} = 2$ (ρ_{Ti} is a thermal ion gyroradius), $s_s = 3$, $q_s = 4$, $\epsilon = 0.1$ in an hydrogen plasma gives $C \simeq 0.9$ - so $C = 1.0$ is kind of an upper bound. As expected, increasing the C parameter is stabilising. This drastic change in stability is due to a stronger relative weight of deeply trapped particles $\theta_b \ll 1$ in the integrals over the bounce angle θ_b, which favors the low θ_b part of the precession frequency $\bar{\Omega}_d$ shown Fig.3. Indeed the precession frequency $\bar{\Omega}_d$, and thus the interchange growth rate, is lower at negative triangularity for $\theta_b \simeq 0$. In absence of FOW effects, this favorable role of negative triangularity is counterbalanced by barely trapped electrons, i.e. near trapped/passing boundary. Barely trapped electrons contribute a lot because they spend a long time near their bounce point, in contrast with deeply trapped particles. Mathematically this feature translates in a $1/\bar{\Omega}_b$ weight in all integrals in λ (or θ_b). This effect is amplified by the behaviour of the function k_d vs the bounce angle θ_b, see Fig.7, which also confers some extra weight to barely trapped particles. When finite orbit width effects are included, these terms are annihilated by a bounce average weight, which is stronger for deeply rather than barely trapped particles. In a nutshell, FOW effects give more weight to deeply trapped particles, thus leading to an inversion of stability between positive and negative triangularities. Since the FOW parameter C increases with both magnetic shear and toroidal wave number n, it is expected that the favourable stabilising effect of negative triangularity should increase with these two parameters, consistently with recent numerical results [16].

The real frequency is shown on Fig.8. Negative triangularity effectively lowers the real angular frequency. It is always positive as it should be, i.e. modes rotate in the same direction as the precession frequency of trapped electrons.

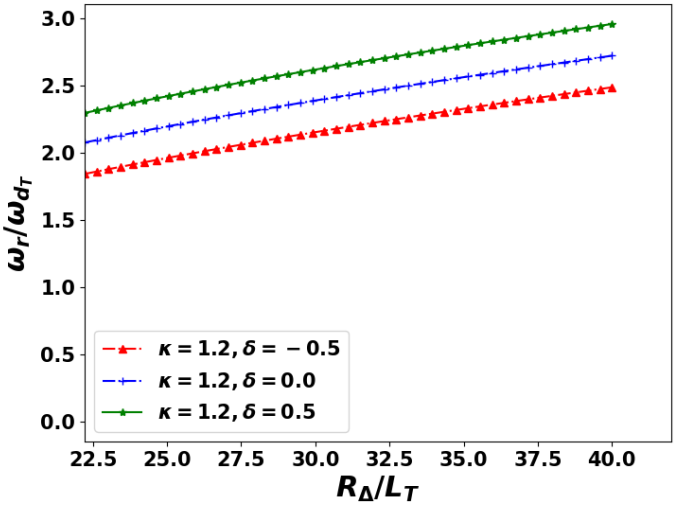

Figure 8: Frequency vs R_Δ/L_T for a triangularity scan $\delta = -0.5$, and $\delta = 0.5$ at fixed elongation $\kappa = 1.2$ with FOW effects included $C = 1.0$.

4.6 Finite mode width effects

The localised character of modes along a field line further amplify FOW effects. Mode structures cannot be calculated with the present simple model, but their impact can be assessed by imposing an ad-hoc shape. Assuming a mode Gaussian shape $\sim \exp(-D\theta^2/2)$, this is equivalent to incorporating a weight function $W^2(\theta_b)$, where $W(\theta_b) = \Gamma_0\left(\frac{D}{2}\theta_b^2\right)$ is the bounce average of the perturbed electric potential, with $\Gamma_0(x) = \exp(-x)I_0(x)$, and I_0 is the modified Bessel function of the first kind and index 0 (see derivation in Appendix C). A rough estimate of D is $D \simeq k_\theta \rho_{Ti}\sqrt{s_s q_s}$, where ρ_{Ti}, hence increases with magnetic shear and poloidal wave number, similarly to the FOW parameter C. Parameter D can thus exceed 1 more easily than C. Average over the bounce angle θ_b (or pitch-angle variable λ), and definition of the effective fraction of trapped particles are then changed accordingly. An example with $D = 1.0$ is shown on Fig.9. It appears that negative triangularity is more stable that its positive counterpart. The frequency is also about the same, i.e. modes drift in the electron diamagnetic direction. Effect increases with D as expected. An example with $D = 2$, is shown on Fig.(10). Note that FOW effects are not included in this calculation at this stage (see next section).

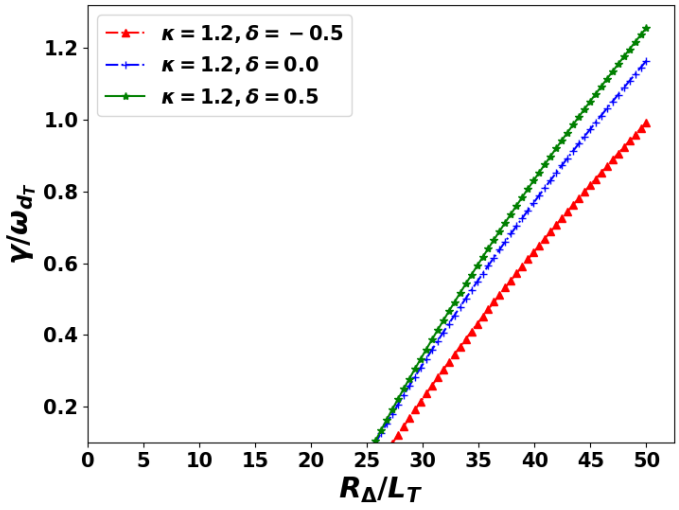

Figure 9: Growth rate vs R_Δ/L_T for a triangularity scan $\delta = -0.5$, $\delta = 0.0$ and $\delta = 0.5$ at fixed elongation $\kappa = 1.2$ with mode width effects $D = 1.0$.

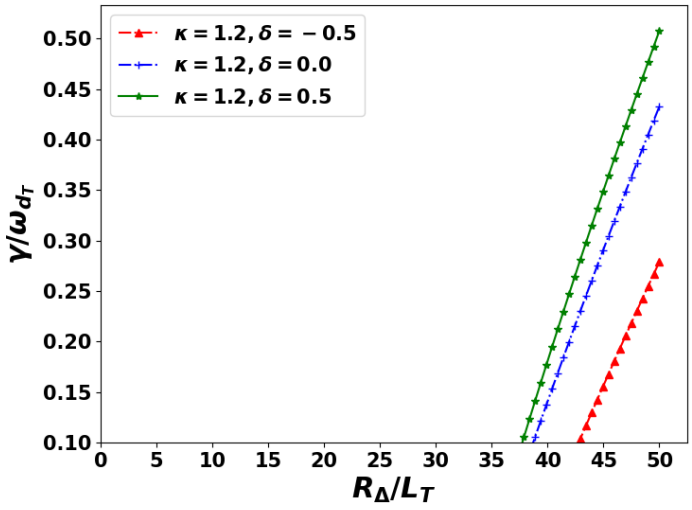

Figure 10: Growth rate vs R_Δ/L_T for a triangularity scan $\delta = -0.5$, $\delta = 0.0$ and $\delta = 0.5$ at fixed elongation $\kappa = 1.2$ with mode width effects $D = 2.0$.

4.7 Inclusion of finite orbit width, finite mode width and collisions

A more general dispersion relation that includes finite orbit and mode width effects, and collisions, is given by

$$1 - \sqrt{\frac{2}{\pi}} \int_{\lambda_-}^{\lambda_+} \frac{d\lambda}{\bar{\Omega}_b} \int_0^{+\infty} d\mathcal{E}\sqrt{\mathcal{E}} e^{-\mathcal{E}} \frac{\hat{\omega}_{*T}\left(\mathcal{E} - \frac{3}{2} + \frac{1}{\eta}\right) - \hat{\omega}}{\bar{\Omega}_d \mathcal{E} - \hat{\omega} - i\hat{\nu}_0 \mathcal{E}^{-3/2}} W^2(\mathcal{E}, \theta_b) = 0$$

where all the frequencies with a hat correspond to the frequencies normalized to ω_{dT}, and $W(\mathcal{E}, \theta_b)$ is given by (see Appendix C)

$$W(\mathcal{E}, \theta_b) = \exp\left(-\frac{D}{2}\theta_b^2\right) I_0\left[\left(D^2 - \frac{\delta_b^2}{d^2}\mathcal{E}\right)^{1/2} \frac{\theta_b^2}{2}\right]$$

An example is shown on Fig.11 with $C = 0.5$ and $D = 0.5$.

Finally the effect of collision is illustrated on Fig.12, for the same parameters and $\nu^* = 0.1$. Here, the collision frequency $\hat{\nu}_0$ is computed from the collisionality ν^* as $\hat{\nu}_0 = \frac{\nu^*}{(k_\theta \rho_i)\sqrt{\frac{m_e}{m_i}} q}$ where $(k_\theta \rho_i)$ has been chosen equal to 1. Collisions are stabilising, as expected for TEMs. Collisions are found to amplify the synergetic effect of FOW/mode localisation with negative triangularity. Values of temperature gradients R_Δ/L_T that are needed to destabilise TEMs are unrealistic for this choice of paramaters. A parameter scan shows that the trend remains the same when C, D become smaller, while the instability threshold gets lower.

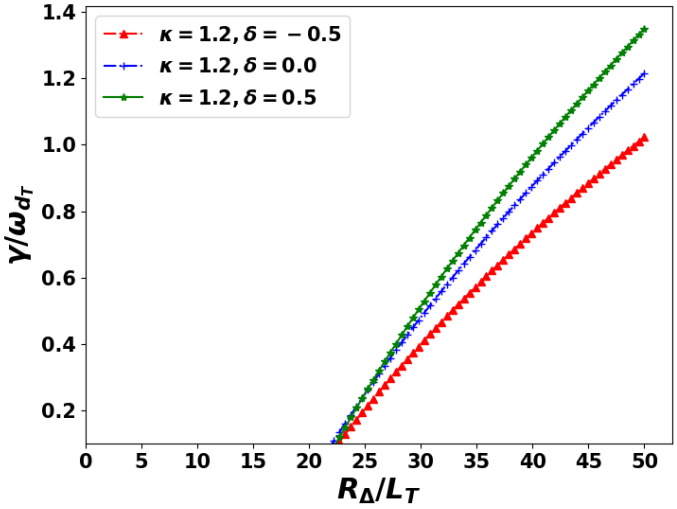

Figure 11: Growth rate vs R_Δ/L_T for a triangularity scan $\delta = -0.5$, $\delta = 0.0$ and $\delta = 0.5$ at fixed elongation $\kappa = 1.2$ with FOW $C = 0.5$ and mode width effects $D = 0.5$ included.

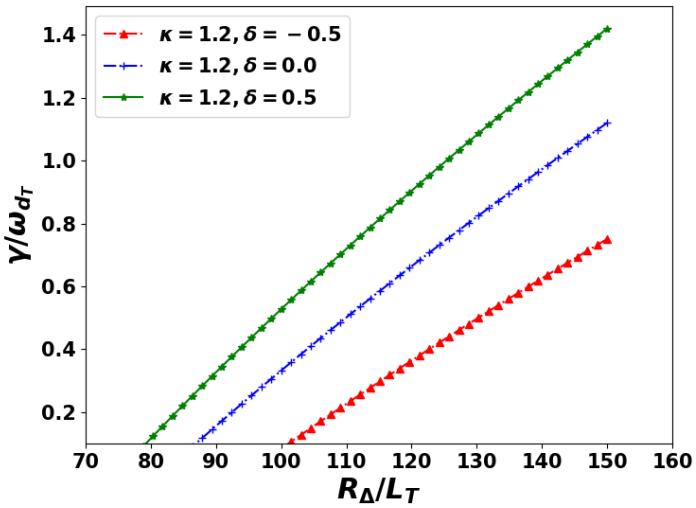

Figure 12: Growth rate vs R_Δ/L_T for a triangularity scan $\delta = -0.5$, $\delta = 0.0$ and $\delta = 0.5$ at fixed elongation $\kappa = 1.2$ with FOW effects $C = 0.5$, FMW effects $D = 0.5$ and collisions included $\nu^* = 0.1$.

5 Conclusion

A reduced model for Trapped Electron Modes (TEMs) stability has been developed, which incorporates basic elements of magnetic surface shaping, in particular elongation and tri-

angularity. It is based on a class of local magnetic equilibria developped by Hegna [27, 28] combined with shapes of magnetic surfaces similar to the class of "Culham equilibria" [32]. This approach allows a fast calculation of bounce and precession frequencies, which can be incorporated in a simplified dispersion relation of TEMs. The advantage of this model is that it allows a detailed investigation of various ingredients that come into play when shaping matters.

This model shows that while elongation is stabilising, though weakly, negative triangularity usually leads to a more unstable situations. This is against observation. This conundrum is solved when finite orbit and/or mode width effects are included. These effects put some weight on the precession frequency at low bounce angles, where negative triangularity produces lower precession frequencies compared with their positive counterparts. As a result, the interchange growth rate becomes lower, leading to stabilisation at large temperature gradients and negative triangularity.

Acknowledgements

The authors thank Prof P.H. Diamond for fruitful discussions at the Festival of Theory, Aix en Provence, France 2021, and also Drs M. Becoulet and G. Huysmans. This work has been carried out within the framework of the EUROfusion Consortium, funded by the European Union via the Euratom Research and Training Programme (Grant Agreement No 101052200 EUROfusion) and from the European Union's Horizon 2020 research and innovation program under Grant Agreement No. 824158 (EoCoE-II). Views and opinions expressed are however those of the author(s) only and do not necessarily reflect those of the European Union or the European Commission. Neither the European Union nor the European Commission can be held responsible for them. This work was supported by the EUROfusion Theory and Advanced Simulation Coordination (E-TASC) initiative under the TSVV-02 (Theory, Simulation, Verification and Validation) "Physics Properties of Strongly Shaped Configurations" project. This research is supported by the National Research Foundation, Singapore.

Appendices

A Explicit expressions of bounce and precession frequencies for a Culham equilibrium

In the special case of a Culham equilibrium, the Hamiltonian frequencies can be computed in a fast and efficient way. The pitch-angle is related to the bounce angle by

$$\lambda = \frac{R_s\left(\theta_b\right)}{R_{max}} = \frac{R_\Delta + \left(r_s - E_s\right)\cos\theta_b + T_s\cos 2\theta_b}{R_\Delta + \left(r_s - E_s\right) + T_s} \tag{26}$$

This equation admits a single positive value of θ_b for small enough values of elongation and triangularity. This condition is equivalent to request that the major radius is a decreasing function of the poloidal angle for $\theta \in [0, \pi] \mod (2\pi)$. More precisely we request that the condition $r_s \geq E_s + 4\|T_s\|$ is fulfilled. The analysis is restrained to this case in the following. The bounce angle is then related to λ by the relationship

$$\cos\theta_b = -\frac{r_s - E_s}{4T_s} + \frac{1}{4T_s}\sqrt{\mathcal{D}} \tag{27}$$

where

$$\mathcal{D} = \left(r_s - E_s\right)^2 + 8T_s\left(\lambda R_{max} - R_\Delta + T_s\right)$$

provided that $\lambda_- \leq \lambda \leq \lambda_+$, where

$$\begin{aligned} \lambda_- &= \frac{B_{min}}{B_{max}} = \frac{R_{min}}{R_{max}} = \frac{R_\Delta - \left(r_s - E_s\right) + T_s}{R_\Delta + \left(r_s - E_s\right) + T_s} \\ \lambda_+ &= 1 \end{aligned}$$

where B_{min} and B_{max} are the minimum and maximum values of the magnetic field on the reference magnetic surface.

Using the relationship $\Omega_b = \bar{\Omega}_b(\lambda)\sqrt{\mathcal{E}}\frac{v_T}{2q_s R_{\max}}$, the normalised bounce frequency is

$$\frac{1}{\bar{\Omega}_b(\lambda)} = \frac{1}{2\pi}\int_{-\theta_b}^{\theta_b} d\theta \frac{R_s^{3/2}(\theta)}{R_{max}} \frac{1}{\sqrt{2\left(R_s(\theta) - R_s(\theta_b)\right)}}$$

The precession frequency $\Omega_d(\lambda)$ is of the form Eq.(14) where

$$\bar{\Omega}_d(\theta_b) = \frac{L_1(\theta_b)}{L_0(\theta_b)}$$

The functions L_0 and L_1 are given by

$$L_0(\theta_b) = \int_0^{\theta_b} \frac{d\theta}{\pi} \frac{R_s^{3/2}(\theta)}{R_{max}} \frac{1}{\sqrt{2\left(R_s(\theta) - R_s(\theta_b)\right)}}$$

and

$$\begin{aligned} L_1(\theta_b) &= \int_0^{\theta_b} \frac{d\theta}{\pi} \frac{R_s^{3/2}(\theta)}{R_{max}} \frac{2-\lambda(\theta_b)b_s(\theta)}{\sqrt{2\left(R_s(\theta)-R_s(\theta_b)\right)}} \\ &\quad \left(\frac{r_s^2}{a_s^2}\frac{\partial Z_s}{r_s\partial\theta} - \left(s_s\theta - \alpha_m\tilde{D}\right)\frac{\partial R_s}{r_s\partial\theta}\right) \\ &- \frac{\alpha_m}{2q_s^2}\lambda(\theta_b)\int_0^{\theta_b}\frac{d\theta}{\pi}\frac{R_s^{3/2}(\theta)}{R_{max}}\frac{b_s(\theta)}{\sqrt{2\left(R_s(\theta)-R_s(\theta_b)\right)}} \end{aligned}$$

Derivatives of (R_s, Z_s) are straightforward

$$\begin{aligned} \frac{\partial R_s}{\partial\theta} &= -\left(r_s - E_s\right)\sin\theta - 2T_s\sin 2\theta \\ \frac{\partial Z_s}{\partial\theta} &= \left(r_s + E_s\right)\cos\theta + 2T_s\cos 2\theta \end{aligned}$$

Let us note the following identity

$$R_s(\theta) - R_s(\theta_b) = \left(\cos\theta - \cos\theta_b\right)\left(r_s - E_s + 2T_s\left(\cos\theta + \cos\theta_b\right)\right)$$

The part $(\cos\theta - \cos\theta_b)$ is responsible for integrable singularities at $\theta = \theta_b$ in the integrals L_0 and L_1, and can be recast as

$$\cos\theta - \cos\theta_b = 2\sin^2\left(\frac{\theta_b}{2}\right)\left(1 - \frac{\sin^2\left(\frac{\theta}{2}\right)}{\sin^2\left(\frac{\theta_b}{2}\right)}\right)$$

The prefactor appears both in L_0 and L_1 and can be removed safely since only the ratio L_1/L_0 matters. One can then perform the usual change of variables

$$\sin v = \frac{1}{\chi}\sin\left(\frac{\theta}{2}\right) \tag{28}$$

where $\chi = \sin\left(\frac{\theta_b}{2}\right)$. The functions L_0 and L_1 then read

$$L_0(\theta_b) = \int_0^{\pi/2}\frac{dv}{\sqrt{1-\chi^2\sin^2 v}}L(\theta,\theta_b)$$

and

$$\begin{aligned} L_1(\theta_b) &= \int_0^{\pi/2}\frac{dv}{\sqrt{1-\chi^2\sin^2 v}}L(\theta,\theta_b)\left[2-\lambda(\theta_b)b_s(\theta)\right] \\ &\times \quad \left(\frac{r_s^2}{a_s^2}\frac{\partial Z_s}{r_s\partial\theta} - \left(s_s\theta - \alpha_m\tilde{D}(\theta)\right)\frac{\partial R_s}{r_s\partial\theta}\right) \\ &- \frac{\alpha_m}{2q_s^2}\lambda(\theta_b)\int_0^{\pi/2}\frac{dv}{\sqrt{1-\chi^2\sin^2 v}}L(\theta,\theta_b)b_s(\theta) \end{aligned} \tag{29}$$

where

$$L(\theta,\theta_b)=\frac{1}{\pi}\frac{R_s^{3/2}(\theta)}{R_{max}}\frac{1}{\sqrt{r_s-E_s+2T_s\left(\cos\theta+\cos\theta_b\right)}}$$

In these expressions, θ must be considered as a function of v, using the change of variables Eq.(28) and the usual trigonometric relations

$$\begin{aligned}\cos(\theta) &= 1-2\chi^2\sin^2 v\\ \sin(\theta) &= 2\chi\sin v\sqrt{1-\chi^2\sin^2 v}\\ \sin(2\theta) &= 2\sin\theta\cos\theta\\ \cos(2\theta) &= 2\cos^2\theta-1\end{aligned}$$

The bounce frequency can also be readily calculated using these definitions

$$\frac{1}{\bar{\Omega}_b(\lambda)}=L_0\left(\theta_b\right)$$

and a fraction of trapped particles accordingly

$$f_t=\int_{\lambda_-}^{\lambda_+}\frac{d\lambda}{\sqrt{2}\bar{\Omega}_b(\lambda)}$$

For passing particles $\lambda\leq\lambda_-$, the normalised transit frequency is

$$\frac{1}{\bar{\Omega}_b(\lambda)}=\frac{1}{2\pi}\int_{-\pi}^{\pi}d\theta\left(\frac{R_s}{R_{max}}\right)^{3/2}\frac{1}{\sqrt{2\left(\frac{R_s}{R_{max}}-\lambda\right)}}$$

It is stressed that for highly passing particles, the effect of shaping is quite small since for $\lambda\to 0$, $\bar{\Omega}_b\to\sqrt{2}$.

B Properties of the G_ϵ function

B.1 Relation of G_ϵ function with plasma dispersion function

We want to compute

$$G_\epsilon(\Omega)=\frac{2}{\sqrt{\pi}}\int_0^{+\infty}d\mathcal{E}\mathcal{E}^{1/2}e^{-\mathcal{E}}\frac{1}{\mathcal{E}-\Omega-i\epsilon}$$

as function of the plasma dispersion function. Here ϵ is a small number which can be positive or negative. Note that the function $\mathcal{E}^{1/2}e^{-\mathcal{E}}$ is holomorphic except on a branch cut, usually chosen along the negative real axis. If ϵ is positive, the function G_ϵ, noted

G_+, is defined in the upper half of the complex plane, then analytically continued in the lower half-plane. In the opposite case $\epsilon < 0$, G_ϵ, noted G_-, is defined in the lower half of the complex plane, then analytically continued in the upper half-plane. First step is to introduce a change of variable on $\mathcal{E}$, then introduce $u = \pm\Omega^{1/2}$. A delicate question is to choose the branch cut on $\Re(\Omega)$ when computing u. A reasonable choice is to choose a branch cut on the semi-axis of negative values of real Ω when $\epsilon > 0$, and half-axis of positive real Ω when $\epsilon < 0$, i.e. $u = \epsilon\Omega^{1/2}$. After a few manipulations, one finds

$$G_\epsilon = 2 + 2u^2 \frac{1}{\sqrt{\pi}} \int_{-\infty}^{+\infty} dv e^{-v^2} \frac{1}{v^2 - u^2}$$

Using

$$\frac{2u}{v^2 - u^2} = \frac{1}{v - u} - \frac{1}{v + u}$$

and changing v in $-v$ in the second integral, one readily finds that

$$G_\epsilon(\Omega) = 2 + 2uZ\left(u\right)$$

where

$$Z(u) = \frac{1}{\sqrt{\pi}} \int_{-\infty}^{+\infty} dv e^{-v^2} \frac{1}{v - u}$$

is the plasma dispersion function. It is reminded that

$$Z(u) = i\sqrt{\pi} e^{-u^2} \text{erfc}(-iu) = i\sqrt{\pi} w(u)$$

where $w(u)$ is the Faddeeva function. Note that the dependence on ϵ is now hidden in the choice of $u = \pm\Omega^{1/2}$. This relation can in fact be recast as $G_\epsilon(\Omega) = -Z'(u)$, where Z' is the derivative of Z. It can be checked that the choice $u = \epsilon\Omega^{1/2}$ is consistent with the expectation from Landau prescription.

B.2 Derivative of the G_ϵ function

Since zeros of the dispersion relation are to be computed, and a Newton-Raphson method is used, it is useful to calculate the first derivative of G_ϵ with respect to Ω

$$\frac{dG_\epsilon}{d\Omega} = -2 + \left(1 - 2u^2\right) \frac{Z\left(u\right)}{u}$$

The derivative of $\mathcal{D}(\Omega)$ is then easily derived

$$\frac{d\mathcal{D}}{d\Omega} = -G_\epsilon - \left(u^2 - \frac{3}{2}\right) \frac{dG_\epsilon}{d\Omega}$$

B.3 Asymptotic expression at large arguments

An expansion at large arguments yield the following expression relation

$$G_\epsilon(\Omega) = -\frac{1}{\Omega}\sum_{n=0}^{+\infty}\frac{\Gamma\left(n+\frac{3}{2}\right)}{\Gamma\left(\frac{3}{2}\right)}\frac{1}{\Omega^n}$$

with Γ the gamma function ($\Gamma\left(\frac{3}{2}\right) = \frac{\sqrt{\pi}}{2}$, $\Gamma\left(z+1\right) = z\Gamma\left(z\right)$). A bit of algebra shows that

$$\left(\Omega - \frac{3}{2}\right)G_\epsilon(\Omega) = -1 - \sum_{n=2}^{+\infty}\left(n-1\right)\frac{\Gamma\left(n+\frac{1}{2}\right)}{\Gamma\left(\frac{3}{2}\right)}\frac{1}{\Omega^n} \tag{30}$$

Similarly

$$\begin{aligned}\left(\Omega\left(1-f_t\epsilon_T\right) - \frac{3}{2} + \frac{1}{\eta}\right)G_\epsilon(\Omega) &= -\left(1-f_t\epsilon_T\right)\\ -\sum_{n=1}^{+\infty}\left[\left(n+\frac{1}{2}\right)\left(1-f_t\epsilon_T\right) - \frac{3}{2} + \frac{1}{\eta}\right]&\frac{\Gamma\left(n+\frac{1}{2}\right)}{\Gamma\left(\frac{3}{2}\right)}\frac{1}{\Omega^n}\end{aligned} \tag{31}$$

C FOW and mode width effect

The structure of FOW and mode width effects is derived here with simple arguments. Let us consider a mode in ballooning formalism, from the ballooning representation of the perturbed electric potential

$$\delta\phi(\alpha,\psi,\theta,t) = \phi_\omega(\alpha,\psi,\theta)\exp\left(-i\omega t\right) + c.c.$$

with

$$\phi_\omega(\alpha,\psi,\theta) = \hat{\phi}_{\mathbf{k}\omega}(\theta)\exp\left(in\alpha + iK_\psi(\psi-\psi_s)\right) \tag{32}$$

where the radial wave number is conveniently rewritten $K_\psi = n\frac{dq}{d\psi}\theta_k$, θ_k the ballooning angle, and (n, K_ψ) are the components of the perpendicular wave number $\mathbf{k}$. In the general case (weakly ballooned modes), this expression can be made periodic in θ thanks to a convolution with a Dirac comb $\sum_{p=-\infty}^{+\infty}\delta(\theta'-\theta-2p\pi)$. For the sake of simplicity, only the strong ballooning limit will be considered.

Eq.(32) can be seen as an eikonal representation $\delta\phi = \hat{\phi}_{\mathbf{k}\omega}(\theta)e^{i\mathcal{S}-i\omega t}$, where $\mathcal{S} = n\alpha + K_\psi(\psi-\psi_s)$ contains the fast variation, thus leading to the definition $\mathbf{k}_\perp = \nabla\mathcal{S}$. Hence assuming zero ballooning angle and strongly ballooned modes, one finds

$$\tilde{\phi}_\omega = \hat{\phi}\left(\theta\right)\exp\left(in\zeta - inq(\psi)\theta\right)$$

Periodicity in θ is not an issue here since $\hat{\phi}(\theta)$ is supposed to be a localised function. Poloidal and toroidal angles of trapped particles are of the form

$$\begin{aligned}\theta &= \hat{\theta}(\alpha_b)\\ \zeta &= \zeta_d + q(\psi_s)\hat{\theta}(\alpha_b) + \hat{\zeta}(\alpha_b)\end{aligned}$$

where δ_b is a banana width, ζ_d the precession angle, $\hat{\delta}, \hat{\theta}, \hat{\zeta}$ are periodic functions of the bounce angle α_b, which also depends on the invariants of motion $E, \theta_b, P_\zeta = -e_a\psi(r_s)$. The angle $\hat{\zeta}$ represents the departure from a uniform precession motion, and is neglected here. The radial displacement $\delta\psi = \psi - \psi_s$ of a trapped particle is prescribed by the invariance of the toroidal kinetic momentum $P_\zeta = -e_a\psi_s = m_a R_s(\theta)v_\parallel(E,\mu,\theta) - e_a\psi$ (it is reminded that in the large aspect ratio approximation, the toroidal field coincides with the field modulus so that $R_s v_\parallel \approx v_\parallel I_s/B_s$), hence $\delta\psi = \frac{m_a}{e_a}R_s(\theta)v_\parallel(E,\mu,\theta)$. The parallel velocity is prescribed by energy conservation, hence

$$v_\parallel = [2\mathcal{E}]^{1/2} v_T \left[1 - \frac{b_s(\theta)}{b_s(\theta_b)}\right]^{1/2}$$

where it is reminded that $b_s = \frac{B_s}{B_{min}} = \frac{R_{max}}{R_s}$.

$$\delta\psi = \frac{m_a}{e_a} v_T \left[2R_s(\theta)\mathcal{E}\right]^{1/2} \left[R_s(\theta) - R_s(\theta_b)\right]^{1/2}$$

Anticipating that deeply particles $\theta_b \ll 1$ principally matter when FOW effects are accounted for, the poloidal angle is just $\hat{\theta} = \theta_b \sin(\alpha_b)$. The radial displacement is obtained via a development of the major radius near $\theta = 0$, i.e. $R_s(\theta) - R_s(\theta_b) = \frac{1}{2}\left.\frac{\partial^2 R_s}{\partial\theta^2}\right|_{\theta=0}(\theta^2 - \theta_b^2)$, so that

$$\delta\psi = \delta_b\sqrt{\mathcal{E}}\hat{\delta}(\alpha_b)$$

where $\delta_b = \frac{m_a}{e_a} v_T \left[R_\Delta\left(r_s - E_s + 4T_s\right)\right]^{1/2}$ is the banana width in ψ unit, and $\hat{\delta} = \theta_b\cos\alpha_b$. Let us note that it depends on elongation and triangularity.

The quantity that matters in the dispersion relation is the square of the modulus of the bounce average of the electric potential, hence the square of

$$\left\langle \tilde{\phi}_\omega \right\rangle_b = \int_0^{2\pi} \frac{d\alpha_b}{2\pi} \hat{\phi}\left(\hat{\theta}\right) \exp\left(-i\frac{\delta_b}{d}\sqrt{\mathcal{E}}\hat{\delta}\hat{\theta}\right)$$

where the safety factor has been linearised and $d^{-1} = n\left.\frac{dq}{d\psi}\right|_{\psi=\psi_s}$ is the inverse of the distance between resonant surfaces. In the case where the mode structure is ignored, i.e. $\hat{\phi}\left(\hat{\theta}\right) = \hat{\phi}_0$ one gets

$$\left\langle \tilde{\phi}_\omega \right\rangle_b = \hat{\phi}_0 J_0\left(\frac{\delta_b}{2d}\sqrt{\mathcal{E}}\theta_b^2\right)$$

Hence $C = \frac{\delta_b}{2d}$ and thus increases with wave number n and magnetic shear $s_s = \frac{dlogq}{dlogr}$.

In the other extreme case where $\delta_b \ll d$, and $\hat{\phi}(\theta) = \hat{\phi}_0 \exp\left(-\frac{D}{2}\theta^2\right)$ then

$$\left\langle \tilde{\phi}_\omega \right\rangle_b = \hat{\phi}_0 \exp\left(-\frac{D}{2}\theta_b^2\right) I_0\left(\frac{D}{2}\theta_b^2\right) = \hat{\phi}_0 \Gamma_0\left(\frac{D}{2}\theta_b^2\right)$$

where I_0 is the modified Bessel function of the first kind and index 0. The Γ_0 function is localised in θ_b, and the dispersion relation should be weighted by its square. A full calculation of the mode structure is beyond the scope of this study. However, it is possible to speculate about the parametric dependencies of the parameter D. If the non adiabatic response of ions rules the mode structure, then it appears that it results from a balance between finite Larmor radius effects, which behave as $k_\perp^2(\theta)\rho_i^2$ (ρ_i a thermal Larmor radius), and parallel gradient, which roughly goes like $\frac{v_{Ti}^2}{\omega^2 q_s^2 R_s^2}\frac{\partial^2}{\partial\theta^2}$, where v_{Ti} is the thermal ion velocity. An estimate of the perpendicular wave number $\mathbf{k}_\perp$ is obtained in the general case (arbitrary ballooning angle) by using the definition $\mathbf{k}_\perp = \nabla\mathcal{S}$, i.e.

$$\mathbf{k}_\perp = n\nabla\alpha + n\frac{dq}{d\psi}\theta_k\nabla\psi$$

and therefore its modulus on the resonant surface

$$k_\perp^2 = n^2\left(|\nabla\alpha_s|^2 + \frac{dq_s}{d\psi}\theta_k\left(\nabla\psi_s\cdot\nabla\alpha_s\right) + \left(\frac{dq_s}{d\psi}\right)^2\theta_k^2|\nabla\psi_s|^2\right)$$

Using calculations developed in [27, 28], one gets

$$k_\perp^2 = n^2\left(\frac{B_s^2}{|\nabla\psi_s|^2}(1+\Lambda^2) + \frac{dq_s}{d\psi}\theta_k B_s\Lambda + \left(\frac{dq_s}{d\psi}\right)^2\theta_k^2|\nabla\psi_s|^2\right)$$

where

$$\Lambda = -\frac{a_s^2}{r_s^2}\left(s_s\theta - \alpha_m\tilde{D}\right)$$

In the large aspect ratio limit, a tractable expression is obtained

$$k_\perp^2 = k_\theta^2\left(\frac{r_s^2}{a_s^2}(1+\Lambda^2) + 2s_s\Lambda\theta_k + \frac{r_s^2}{a_s^2}s_s^2\theta_k^2\right)$$

Balancing $k_\perp^2(\theta)\rho_i^2$ with $\frac{v_{Ti}^2}{\omega^2 q_s^2 R_s^2}\frac{\partial^2}{\partial\theta^2}$ is expected to yield a solution that approximately behaves as a Gaussian $\exp(-D\theta^2/2)$. A back of the envelope calculation based on the estimate $\omega \simeq \omega_{dT}$ yields $D \simeq k_\theta\rho_{Ti}\sqrt{s_s q_s}$, where ρ_{Ti} is the thermal ion gyroradius. Hence the D parameter is expected to increase with the magnetic shear s_s and poloidal wave number $k_\theta = \frac{nq_s}{r_s}$, similarly to the FOW bounce average term. These two effects are therefore cumulative.

In the general case, the bounce average potential is $\left\langle \tilde{\phi}_\omega \right\rangle_b = \hat{\phi}_0 W(\mathcal{E}, \theta_b)$, where the function W is given by

$$\begin{aligned} W(\mathcal{E}, \theta_b) &= \exp\left(-\frac{D}{2}\theta_b^2\right) \\ &\quad \int_0^{2\pi} \frac{d\alpha_b}{2\pi} \exp\left[\left(-i\frac{\delta_b}{d}\sqrt{\mathcal{E}}\sin(2\alpha_b) + D\cos(2\alpha_b)\right)\frac{\theta_b^2}{2}\right] \\ &= \exp\left(-\frac{D}{2}\theta_b^2\right) I_0\left[\left(D^2 - \frac{\delta_b^2}{d^2}\mathcal{E}\right)^{1/2}\frac{\theta_b^2}{2}\right] \end{aligned}$$

where I_0 is the modified Bessel function of the first kind, index 0, and complex argument (choice of branch for the square root does not matter since I_0 is an even function of its argument). Previous expressions are recovered in the asymptotic cases, i.e. respectively $D = 0$ and $\delta_b = 0$. The square of the bounce average potential contributes to the resonant response, hence $W^2(\mathcal{E}, \theta_b)$.

References

[1] R. E. Waltz and R. L. Miller. Ion temperature gradient turbulence simulations and plasma flux surface shape. Physics of Plasmas, 6(11):4265–4271, 11 1999.

[2] E. A. Belli, G. W. Hammett, and W. Dorland. Effects of plasma shaping on nonlinear gyrokinetic turbulence. Physics of Plasmas, 15(9):092303, 2008.

[3] G. Rewoldt, W. M. Tang, and M. S. Chance. Electromagnetic kinetic toroidal eigenmodes for general magnetohydrodynamic equilibria. The Physics of Fluids, 25(3):480–490, 03 1982.

[4] J Anderson, H Nordman, and J Weiland. Effects of non-circular tokamak geometry on ion-temperature-gradient driven modes. Plasma Physics and Controlled Fusion, 42(5):545, may 2000.

[5] P. Angelino, X. Garbet, L. Villard, A. Bottino, S. Jolliet, Ph. Ghendrih, V. Grandgirard, B. F. McMillan, Y. Sarazin, G. Dif-Pradalier, and T. M. Tran. Role of plasma elongation on turbulent transport in magnetically confined plasmas. Phys. Rev. Lett., 102:195002, May 2009.

[6] M. N. Rosenbluth and F. L. Hinton. Poloidal flow driven by ion-temperature-gradient turbulence in tokamaks. Phys. Rev. Lett., 80:724–727, Jan 1998.

[7] A. Pochelon, T.P. Goodman, M. Henderson, C. Angioni, R. Behn, S. Coda, F. Hofmann, J.-P. Hogge, N. Kirneva, A.A. Martynov, J.-M. Moret, Z.A. Pietrzyk, F. Porcelli, H. Reimerdes, J. Rommers, E. Rossi, O. Sauter, M.Q. Tran, H. Weisen, S. Alberti, S. Barry, P. Blanchard, P. Bosshard, R. Chavan, B.P. Duval, Y.V. Esipchuck,

D. Fasel, A. Favre, S. Franke, I. Furno, P. Gorgerat, P.-F. Isoz, B. Joye, J.B. Lister, X. Llobet, J.-C. Magnin, P. Mandrin, A. Manini, B. Marletaz, P. Marmillod, Y. Martin, J.-M. Mayor, J. Mlynar, C. Nieswand, P.J. Paris, A. Perez, R.A. Pitts, K.A. Razumova, A. Refke, E. Scavino, A. Sushkov, G. Tonetti, F. Troyon, W. Van Toledo, and P. Vyas. Energy confinement and mhd activity in shaped tcv plasmas with localized electron cyclotron heating. Nuclear Fusion, 39(11Y):1807, nov 1999.

[8] Y. Camenen, A. Pochelon, R. Behn, A. Bottino, A. Bortolon, S. Coda, A. Karpushov, O. Sauter, G. Zhuang, and the TCV team. Impact of plasma triangularity and collisionality on electron heat transport in tcv l-mode plasmas. Nuclear Fusion, 47(7):510, jun 2007.

[9] A Marinoni, S Brunner, Y Camenen, S Coda, J P Graves, X Lapillonne, A Pochelon, O Sauter, and L Villard. The effect of plasma triangularity on turbulent transport: modeling tcv experiments by linear and non-linear gyrokinetic simulations. Plasma Physics and Controlled Fusion, 51(5):055016, mar 2009.

[10] G Merlo, S Brunner, O Sauter, Y Camenen, T Görler, F Jenko, A Marinoni, D Told, and L Villard. Investigating profile stiffness and critical gradients in shaped tcv discharges using local gyrokinetic simulations of turbulent transport. Plasma Physics and Controlled Fusion, 57(5):054010, apr 2015.

[11] M. Becoulet, G.T.A. Huijsmans, X. Garbet, P. Donnel, W. Lian, H. Guangzhou, A. Marinoni, and L. Kripner. Nonlinear gyrokinetic ion temperature gradient and trapped electron modes turbulence modelling in x point geometry with 3d fields edge localized modes and at negative and positive triangularity shapes. 29th IAEA Fusion Energy Conference, London, 2023.

[12] M. E. Austin, A. Marinoni, M. L. Walker, M. W. Brookman, J. S. deGrassie, A. W. Hyatt, G. R. McKee, C. C. Petty, T. L. Rhodes, S. P. Smith, C. Sung, K. E. Thome, and A. D. Turnbull. Achievement of reactor-relevant performance in negative triangularity shape in the diii-d tokamak. Phys. Rev. Lett., 122:115001, Mar 2019.

[13] A. Marinoni, M. E. Austin, A. W. Hyatt, M. L. Walker, J. Candy, C. Chrystal, C. J. Lasnier, G. R. McKee, T. Odstril, C. C. Petty, M. Porkolab, J. C. Rost, O. Sauter, S. P. Smith, G. M. Staebler, C. Sung, K. E. Thome, A. D. Turnbull, and L. Zeng. H-mode grade confinement in l-mode edge plasmas at negative triangularity on diii-d. Physics of Plasmas, 26(4):042515, 2019.

[14] A. Marinoni, M.E. Austin, A.W. Hyatt, S. Saarelma, F. Scotti, Z. Yan, C. Chrystal, S. Coda, F. Glass, J.M. Hanson, A.G. McLean, D.C. Pace, C. Paz-Soldan, C.C. Petty, M. Porkolab, L. Schmitz, F. Sciortino, S.P. Smith, K.E. Thome, F. Turco, and the DIII-D Team. Diverted negative triangularity plasmas on diii-d: the benefit of high confinement without the liability of an edge pedestal. Nuclear Fusion, 61(11):116010, sep 2021.

[15] J. M. Duff, B. J. Faber, C. C. Hegna, M. J. Pueschel, and P. W. Terry. Effect of triangularity on ion-temperature-gradient-driven turbulence. Physics of Plasmas, 29(1):012303, 2022.

[16] Gabriele Merlo and Frank Jenko. Interplay between magnetic shear and triangularity in ion temperature gradient and trapped electron mode dominated plasmas. Journal of Plasma Physics, 89(1):905890104, 2023.

[17] Gabriele Merlo, Mattia Dicorato, Bryce Allen, Tilman Dannert, Kai Germaschewski, and Frank Jenko. On the effect of negative triangularity on ion temperature gradient turbulence in tokamaks. Physics of Plasmas, 30(10):102302, 10 2023.

[18] Rameswar Singh and P.H. Diamond. Zonal flow screening in negative triangularity tokamaks. Nuclear Fusion, 62(12):126073, nov 2022.

[19] Rameswar Singh, P.H. Diamond, and A.O. Nelson. Geometric dependencies of the mean exb shearing rate in negative triangularity tokamaks. Nuclear Fusion, 63(12):126053, nov 2023.

[20] B. B. Kadomtsev and O. P. Pogutse. Plasma instability due to particle trapping in a toroidal geometry. JETP, 6:1172, 1967.

[21] Tilman Dannert and Frank Jenko. Gyrokinetic simulation of collisionless trapped-electron mode turbulence. Physics of Plasmas, 12(7):072309, 07 2005.

[22] Jianying Lang, Yang Chen, and Scott E. Parker. Gyrokinetic df particle simulation of trapped electron mode driven turbulence. Physics of Plasmas, 14(8):082315, 08 2007.

[23] Jianying Lang, Scott E. Parker, and Yang Chen. Nonlinear saturation of collisionless trapped electron mode turbulence: Zonal flows and zonal density). Physics of Plasmas, 15(5):055907, 03 2008.

[24] F. Merz and F. Jenko. Nonlinear saturation of trapped electron modes via perpendicular particle diffusion. Phys. Rev. Lett., 100:035005, Jan 2008.

[25] D. R. Ernst, J. Lang, W. M. Nevins, M. Hoffman, Y. Chen, W. Dorland, and S. Parker. Role of zonal flows in trapped electron mode turbulence through nonlinear gyrokinetic particle and continuum simulationa). Physics of Plasmas, 16(5):055906, 05 2009.

[26] Yong Xiao and Zhihong Lin. Turbulent transport of trapped-electron modes in collisionless plasmas. Phys. Rev. Lett., 103:085004, Aug 2009.

[27] C. C. Hegna. Local three-dimensional magnetostatic equilibria. Physics of Plasmas, 7(10):3921–3928, 2000.

[28] C. C. Hegna. The effect of three-dimensional fields on bounce averaged particle drifts in a tokamak. Physics of Plasmas, 22(7):072510, 2015.

[29] R. L. Miller, M. S. Chu, J. M. Greene, Y. R. Lin-Liu, and R. E. Waltz. Noncircular, finite aspect ratio, local equilibrium model. Physics of Plasmas, 5(4):973–978, 1998.

[30] N. Luc C. Mercier. Report No. EUR-5127e 140. European Communities, Brussels, 1974.

[31] Zhangsheng Huang, Weixin Guo, and Lu Wang. The synergetic effects of three-dimensional magnetic perturbations and finite beta on collisionless trapped electron mode in tokamak plasmas. Nuclear Fusion, 62(6):066044, apr 2022.

[32] J. W. Connor and R. J. Hastie. Report No. CLM-M106. Culham Laboratory Report, 1985.

[33] R Fitzpatrick, C G Gimblett, and R J Hastie. On the '11/2-d' evolution of tokamak plasmas in the case of large aspect ratio. Plasma Physics and Controlled Fusion, 34(2):161, feb 1992.

[34] Fabio Riva, Emmanuel Lanti, Sébastien Jolliet, and Paolo Ricci. Plasma shaping effects on tokamak scrape-off layer turbulence. Plasma Physics and Controlled Fusion, 59(3):035001, jan 2017.

[35] A. H. Boozer. Physics of magnetically confined plasmas. Rev. Mod. Phys., 76:1071–1141, 2005.

[36] Per Helander. Theory of plasma confinement in non-axisymmetric magnetic fields. Reports on Progress in Physics, 77(8):087001, jul 2014.

[37] J. W. Connor, R. J. Hastie, and J. B. Taylor. Shear, periodicity, and plasma ballooning modes. Phys. Rev. Lett., 40:396–399, Feb 1978.

[38] C. Bourdelle, G.T. Hoang, X. Litaudon, C.M. Roach, and T. Tala. Impact of the alpha parameter on the microstability of internal transport barriers. Nuclear Fusion, 45(2):110, feb 2005.

[39] F. Romanelli and S. Briguglio. Toroidal semicollisional microinstabilities and anomalous electron and ion transport. Physics of Fluids B: Plasma Physics, 2(4):754–763, 04 1990.